Electronic Supplementary Information

Sustainable ammonia synthesis from the air by the integration of plasma and electrocatalysis techniques

Jun Ding,‡[ab] Wenyi Li,‡*[ab] Qingqing Chen,[c] Jiafang Liu,[ab] Shu Tang,[ab] Zhiwei Wang,[d] Longwei Chen,*[d] and Haimin Zhang*[ab]

[a] Key Laboratory of Materials Physics, Centre for Environmental and Energy Nanomaterials, Anhui Key Laboratory of Nanomaterials and Nanotechnology, Institute of Solid State Physics, HFIPS, Chinese Academy of Sciences, Hefei 230031, China.

[b] University of Science and Technology of China, Hefei 230026, China.

[c] Laboratory of Functional Molecular Solids, Ministry of Education, College of Chemistry and Materials Science, Anhui Normal University Wuhu, 241002, China.

[d] Institute of Energy, Hefei Comprehensive National Science Center, Hefei 230031, China.

* Corresponding Authors.

‡ The authors contributed equally to this work.

E-mail: park0301@mail.ustc.edu.cn, chenlw@ie.ah.cn, zhanghm@issp.ac.cn.

Experimental Section

Reagents and materials: Copper acetylacetonate [$Cu(acac)_2$, 98%], Platinum (II) acetylacetonate [$Pt(acac)_2$, 98%], L-Glutamic acid (95.0%), analytical grade ethanol and isopropanol were purchased from Sinopharm Chemical Reagent Co., Ltd. (Shanghai, China). Oleylamine (approximate C18-content 80-90%) and Dimethyldi-n-octadecylammonium chloride (DODAC, 96.0%) were acquired from Aladdin Industrial Corp. Nafion (5%) was purchased from Sigma Aldrich. Vulcan XC-72R was purchased from Cabot Corporation. Commercial carbon cloth was purchased from Shanghai Hesen Electric Co. Ltd. All available chemicals were used without further purification. All solutions were prepared using deionized water (Millipore Corp, 18.2 MΩ cm).

Characterization: TEM images were obtained using JEMARM 200F operating at an accelerating voltage of 200 kV. The crystalline phase of collected samples were characterized through XRD technique on a Philips X'Pert Pro X-ray diffractometer with Cu Kα radiation (Kα= 0.15418 nm). X-ray photoelectron spectroscopy (XPS) spectra were carried out on ESCALab MKII with Al Kα radiation. The binding energies were calibrated by C 1s peak at 284.8 eV as a reference. Fourier transform infrared (FT-IR) spectra of samples were recorded on Thermo Nicolet NEXUS FT-IR spectrophotometer at room temperature. The content of each element in the catalysts was determined by the inductively coupled plasma mass spectrometry (ICP-MS, 710-ES, Varian). The UV-Vis absorption spectra were carried out on UV-Vis spectrophotometer (SHIMADZU UV-2700). Electron Spin Resonance (ESR)

measurement was conducted by Bruker EMX plus 10/12 (equipped with Oxford ESR910 Liquid Helium cryostat). The H_2 content was determined by online gas chromatography (GC-9790Plus, FULI INSTRUMENTS) thermal conductivity detector (TCD).

Calculation of energy requirement (ER):

The energy requirement (ER) was calculated as follows:

$$ER_{totle} = ER_{plasma} + ER_{electro} \quad (S1)$$

$$ER_{plasma} = (P_G + P_M \times R_d) \times t_{plasma} / \{(c_{NO2-}) \times V_{ab}\} \quad (S2)$$

$$ER_{electro} = P_{electro} \times (n_{NH3} / R_{NH3}) \quad (S3)$$

Where ER_{totle} is the total energy requirement (kWh mol_{NH3}^{-1}), ER_{plasma} is the energy requiremen (kWh mol^{-1}) which convert air into NO_x^- by plasma, $ER_{electro}$ is the energy requiremen (kWh mol^{-1}) which convert NO_2^- into NH_3 by electrocatalysis. P_G is the gliding arc power (400 W), P_M is the microwave power (960 W), R_d is the duty cycle of pulse modulation (1/2), t_{plasma} is the plasma treatment time (h). c_{NO2-} is the concentration of NO_2^- (mol mL^{-1}) and V_{ab} is the volume of absorption liquid (200 mL). $P_{electro}$ is the actual electrocatalysis power (0.004 W), n_{NH3} is the molar mass (mol) of NH_3, R_{NH3} is the ammonia production rate of the electrocatalytic reaction (mol h^{-1}).

Determination of NO_2^-: 20 g of p-aminobenzenesulfonamide was added to a mixed solution of 250 mL of water and 50 mL of phosphoric acid, and then 1 g of N-(1- naphthyl)-ethylenediamine dihydrochloride was dissolved in the above solution. Finally, the above solution was transferred to a 500 mL volumetric flask and diluted to the mark. 0.5 mL

electrolyte was taken out from the electrolytic cell and diluted to 10 mL with H_2O. Next, 0.2 mL color reagent was added into the above mentioned 10 mL solution. After shaking and standing for 30 minutes, the absorbance measurements were performed at wavelength of 540 nm. The concentration-absorbance curves were calibrated using standard KNO_2 solutions with a series of concentrations in 1.0 M KOH solution and the obtained calibration curve ($y=3.183x+0.003$, $R^2=0.999$) shown in Fig. S3 was used to calculate the produced NO_2^--N concentration.

Determination of NO_3^-: The possible produced NO_3^- was detected by ion-chromatography (Wayeal, IC6000) measurement. In detail, 1.0 mL electrolyte was injected into the chamber for separation. The concentration-peak area curves were calibrated using standard KNO_3 solutions with a series of concentrations in 1.0 M KOH solution, in which the peak appeared at a retention time of 13.12 min. The obtained calibration curve ($y=28.343x+0.342$, $R^2=0.998$) shown in Fig. S4 was used to calculate the NO_3^- concentration.

In addition to this method, the possible produced NO_3^- was detected by ultraviolet spectroscopy. For testing, 10 mL of electrolyte was transferred to colorimetric tube with, 200 μL of 1.0 M HCl and 200 μL of 0.8 wt % sulfamic acid solution. The UV-Vis absorption spectrum was detected at a wavelength of 220 nm and 275 nm after maintaining at room temperature for 20 min. The final absorbance is calculated using the following formula: $A=A220_{nm}-2A275_{nm}$. The obtained calibration curve was used to calculate the nitrate concentration. The concentration-absorbance curves were calibrated using standard KNO_3

solutions with a series of concentrations in 1.0 M KOH solution and the obtained calibration curve ($y=0.060x+0.014$, $R^2=0.997$) shown in Fig. S5 was used to calculate the produced NO_3^- concentration.

Determination of ammonia: Concentration of the produced ammonia was spectrophotometrically detected by the indophenol blue method. Briefly, 5.0 g sodium potassium tartrate and 5.0 g sodium salicylate were dissolved in 100.0 mL of 1.0 M sodium hydroxide to prepare the chromogenic reagent (reagent A). 5 mL sodium hypochlorite (10% ~ 15% effective chlorine) was added to deionized water to dilute to 50 mL to prepare the oxidizing reagent (reagent B) The catalytic reagent (reagent C) was prepared by sodium 0.5 g nitroferricyanide dissolved in 50 mL deionized water.

To quantitatively determine the amount of ammonia, 0.5 mL of diluted sample solution was added to a test tube and volume it to 10 mL with deionized water, then 0.5 mL reagent A, 0.2 mL reagent B and 0.20 mL reagent C were successively added, respectively. Following mixing and left-standing for 1 h the UV-Vis absorption spectrum was detected at a wavelength of 697.5 nm at room temperature. The concentration-dependent absorption spectra were calibrated using standard ammonia chloride solutions with varying concentration. The obtained calibration curve ($y=1.033x+0.015$, $R^2=0.999$) shown in Fig. S12 was used to calculate the produced ammonia concentration.

Determination of hydrazine: The possible produced hydrazine was detected through the Watt and Chrisp method. Briefly, 30 mL of HCl, 5.99 g of para-(dimethylamino)

benzaldehyde and 300 mL of ethanol were mixed and used as a sensitive chromogenic reagent. Then, 0.1 mL of solution product was mixed with 5 mL of the chromogenic reagent and 10 mL HCl (1.0 M) at room temperature. After standing for 20 min, the UV-Vis absorption spectrum was measured at a wavelength of 455 nm. The obtained calibration curve ($y=0.019x+0.014$, $R^2=0.999$) shown in Fig. S13 was used to calculate the $N_2H_4 \cdot H_2O$ concentration.

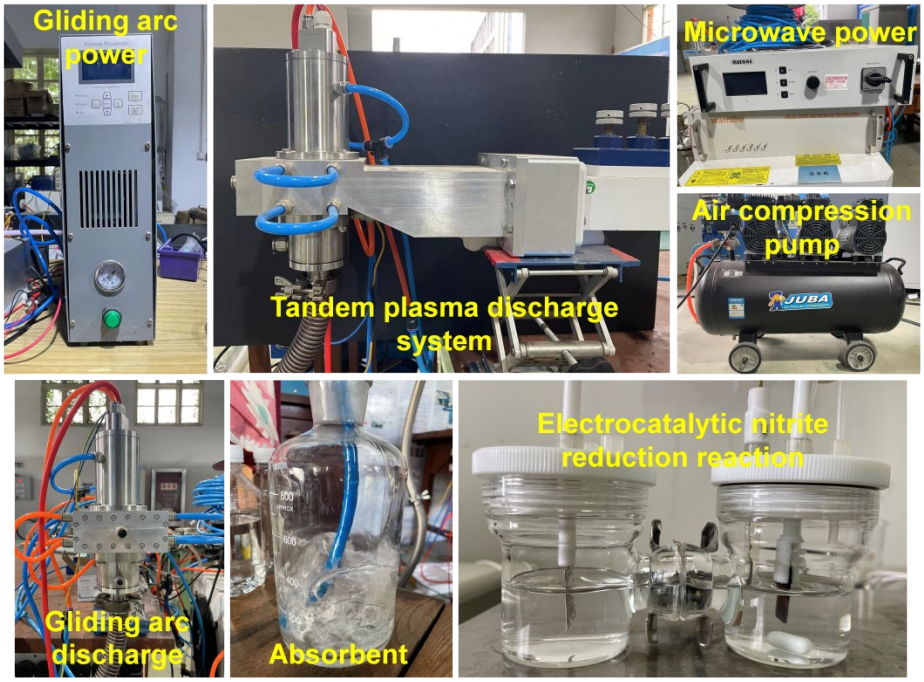

Fig. S1 Photograph of the self-assembly non-thermal plasma (NTP) system.

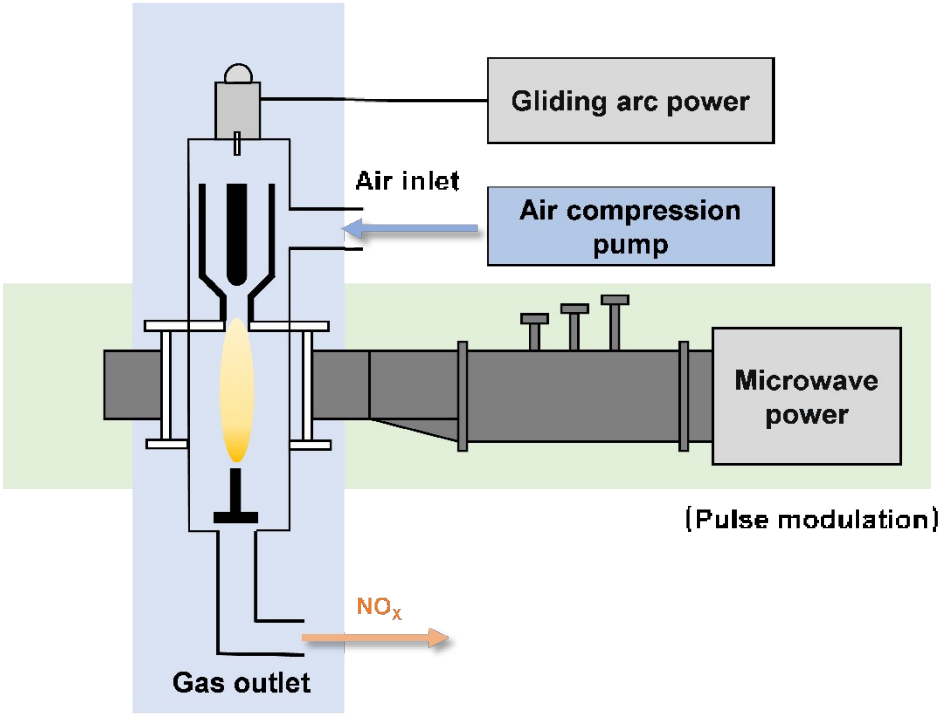

Fig. S2 Schematic illustration of the tandem plasma reactor.

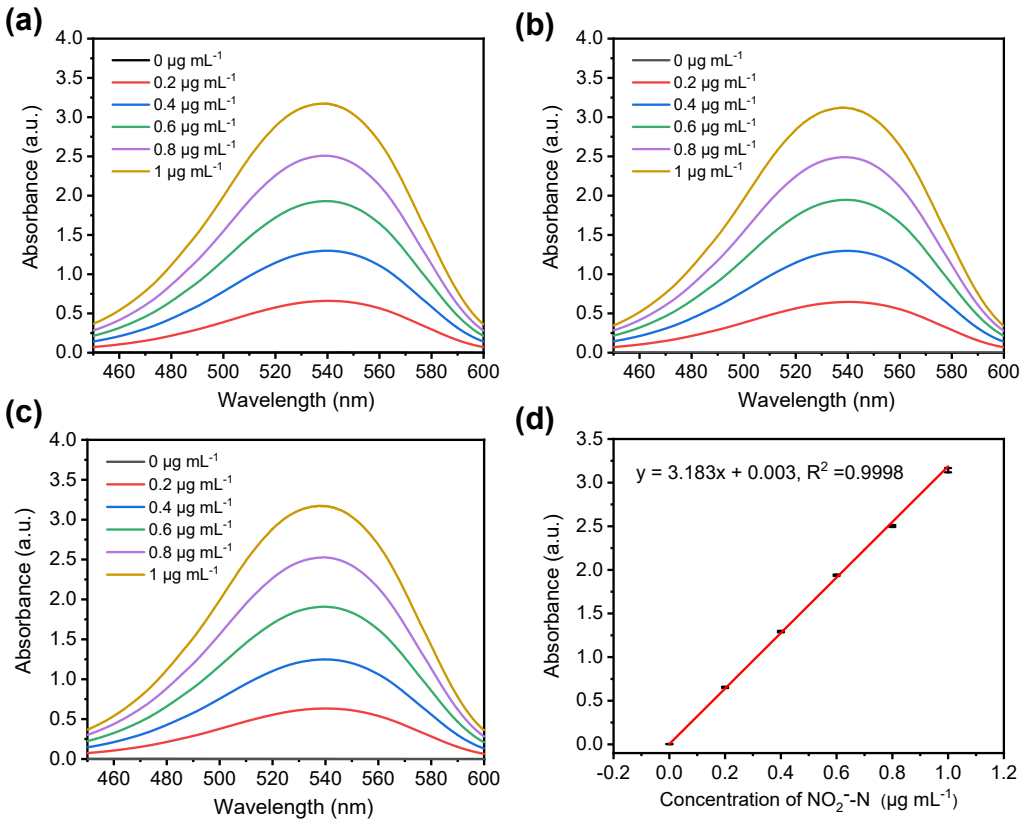

Fig. S3 (a-c) UV-Vis absorption spectra of various NO_2^--N concentrations for three repeated experiments. (d) Calibration curve used for estimation of NO_2^--N concentration.

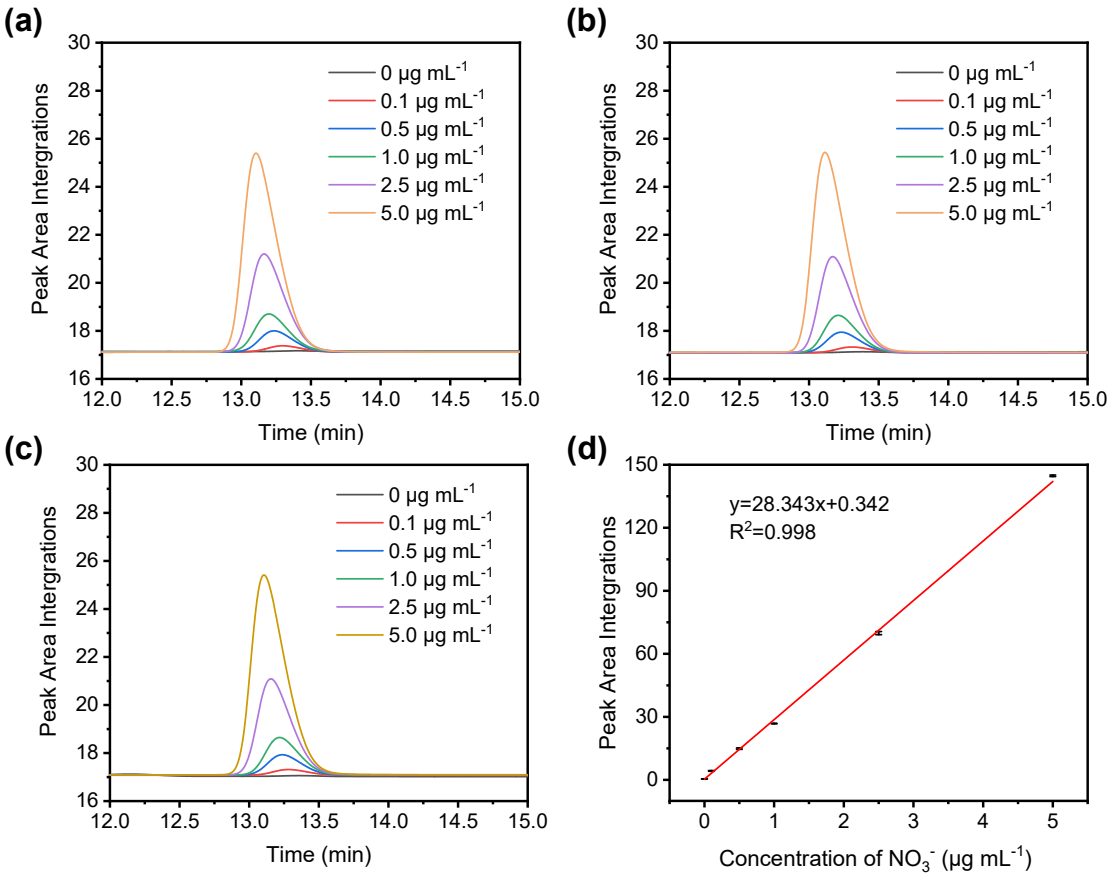

Fig. S4 (a-c) Ion chromatogram spectra of the standard solutions with different concentrations of NO_3^- for three replicated tests. (d) The calibration curve used for calculation of NO_3^- concentration.

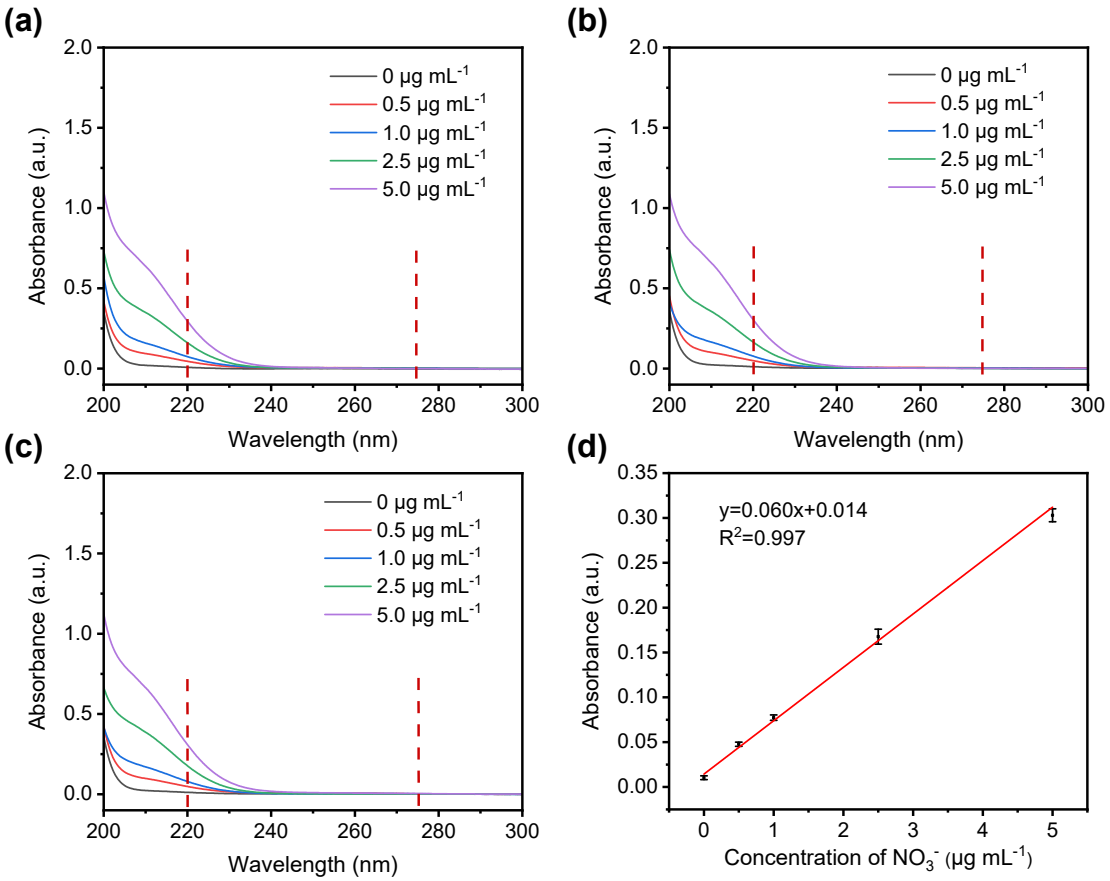

Fig. S5 (a-c) UV-Vis absorption spectra of the standard solutions with different concentrations of NO_3^- for three replicated tests. (d) The calibration curve used for calculation of NO_3^- concentration.

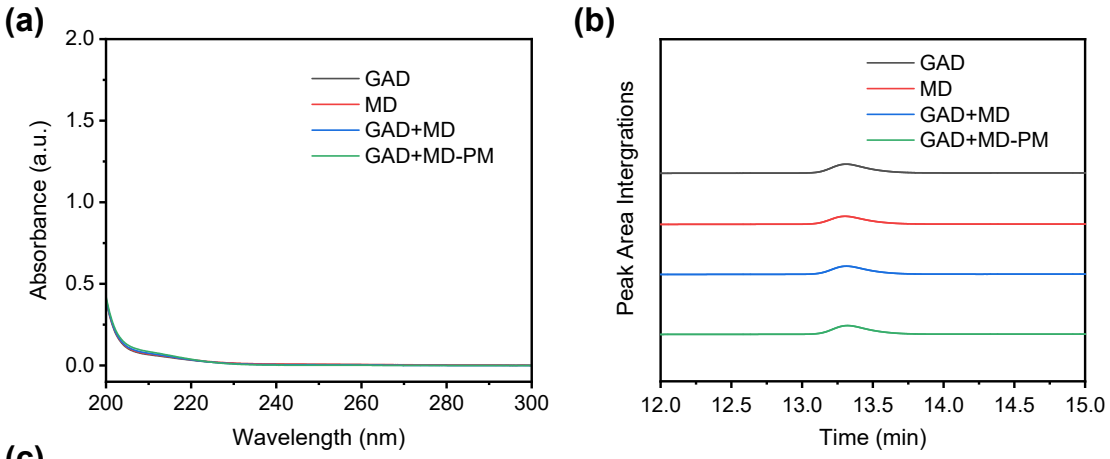

(c)

	GAD	MD	GAD+MD	GAD+MD-PM
Ion chromatography	0.29 μg mL^{-1}	0.30 μg mL^{-1}	0.31 μg mL^{-1}	0.33 μg mL^{-1}
UV-Vis	0.33 μg mL^{-1}	0.25 μg mL^{-1}	0.35 μg mL^{-1}	0.40 μg mL^{-1}

Fig. S6 (a) UV-Vis absorption spectra and (b) ion chromatogram spectra of collected samples obtained at different plasma-activation modes for NO_3^- detection. (c) The comparison table of NO_3^- concentration of the two detection methods under different plasma discharge modes.

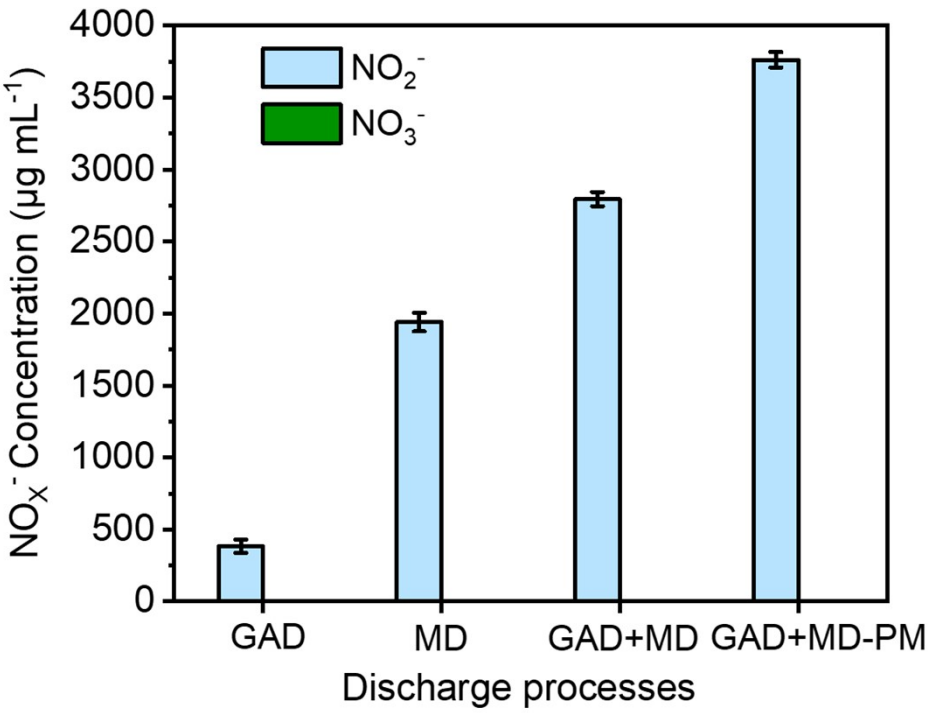

Fig. S7 Comparison of NO_2^- and NO_3^-concentration under different plasma discharge modes.

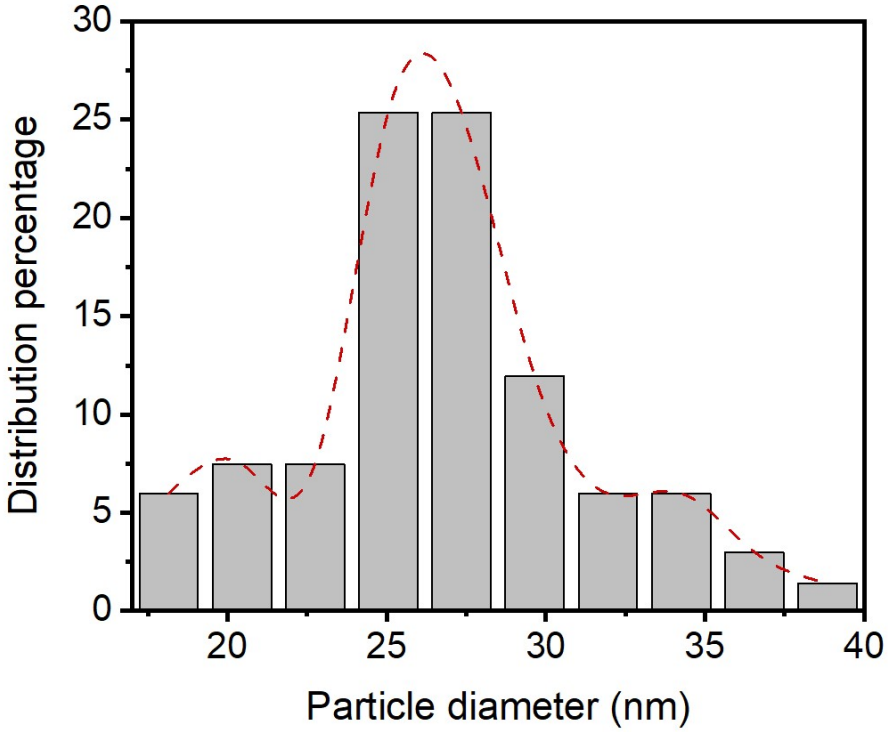

Fig. S8 The particle size distributions of PtCu HPs.

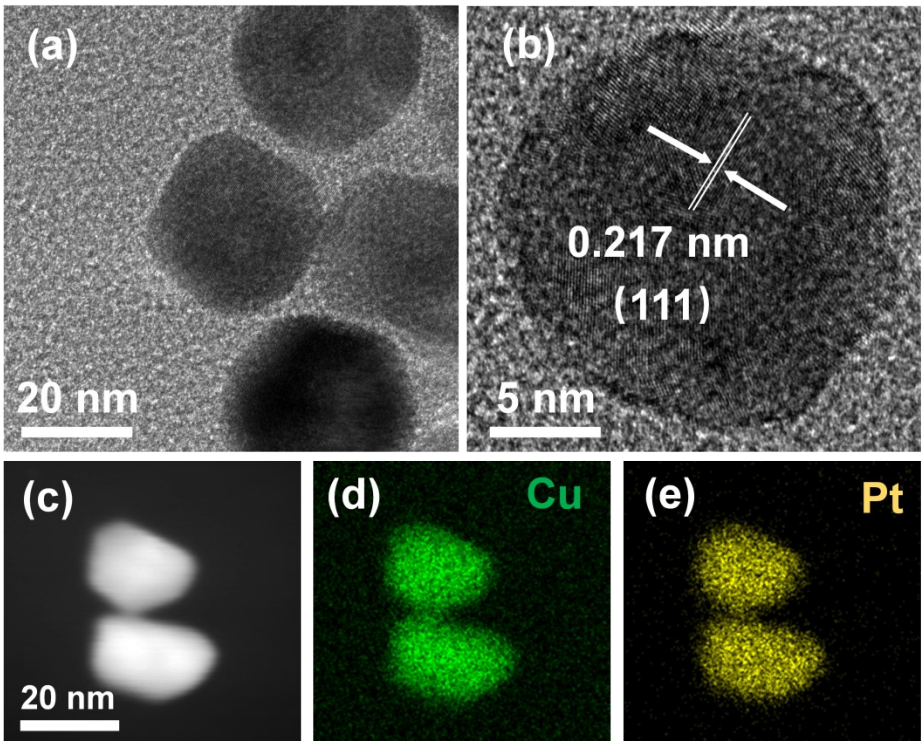

Fig. S9 (a) Low-magnification TEM image, (b) high-resolution TEM image of PtCu NPs, (c-e) HAADF-STEM image and corresponding element mappings of PtCu NPs.

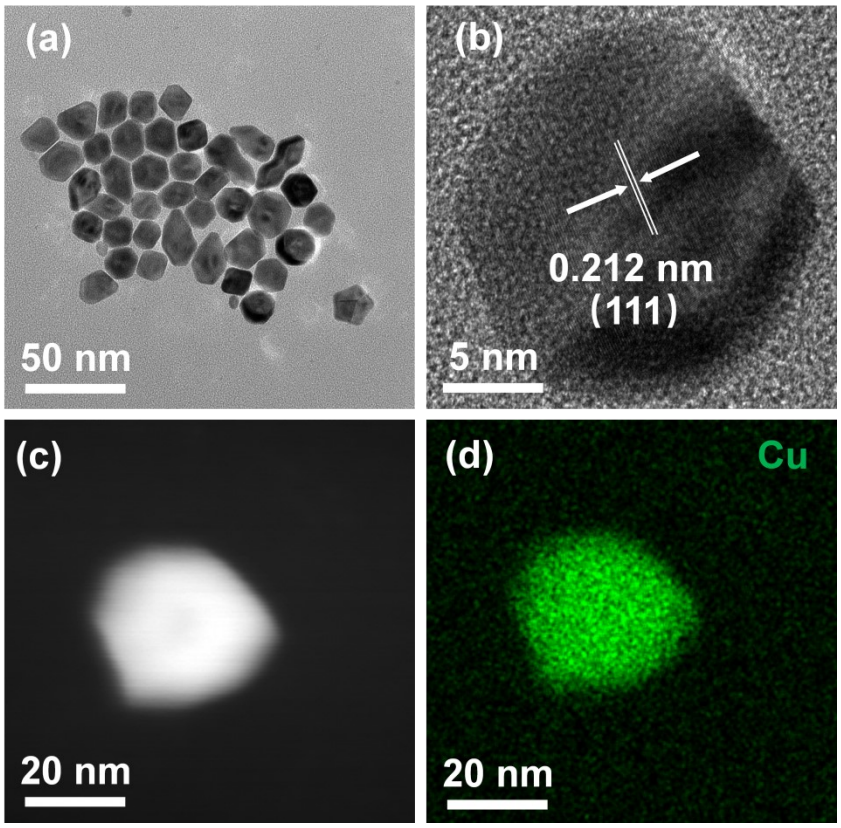

Fig. S10 (a) Low-magnification TEM image, (b) high-resolution TEM image of Cu NPs, (c-d) HAADF-STEM image and corresponding element mappings of Cu NPs.

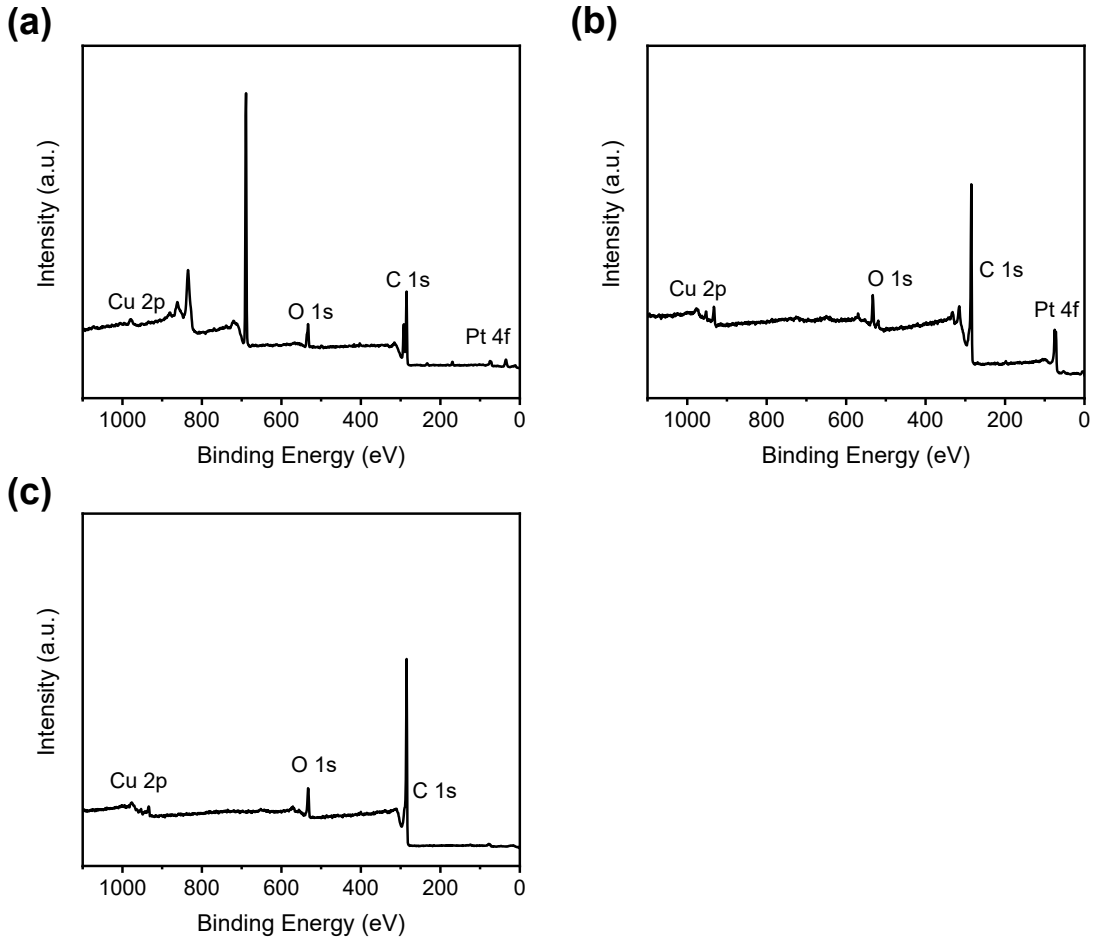

Fig. S11 The surface survey XPS spectra of (a) PtCu HPs, (b) PtCu NPs and (c) Cu NPs.

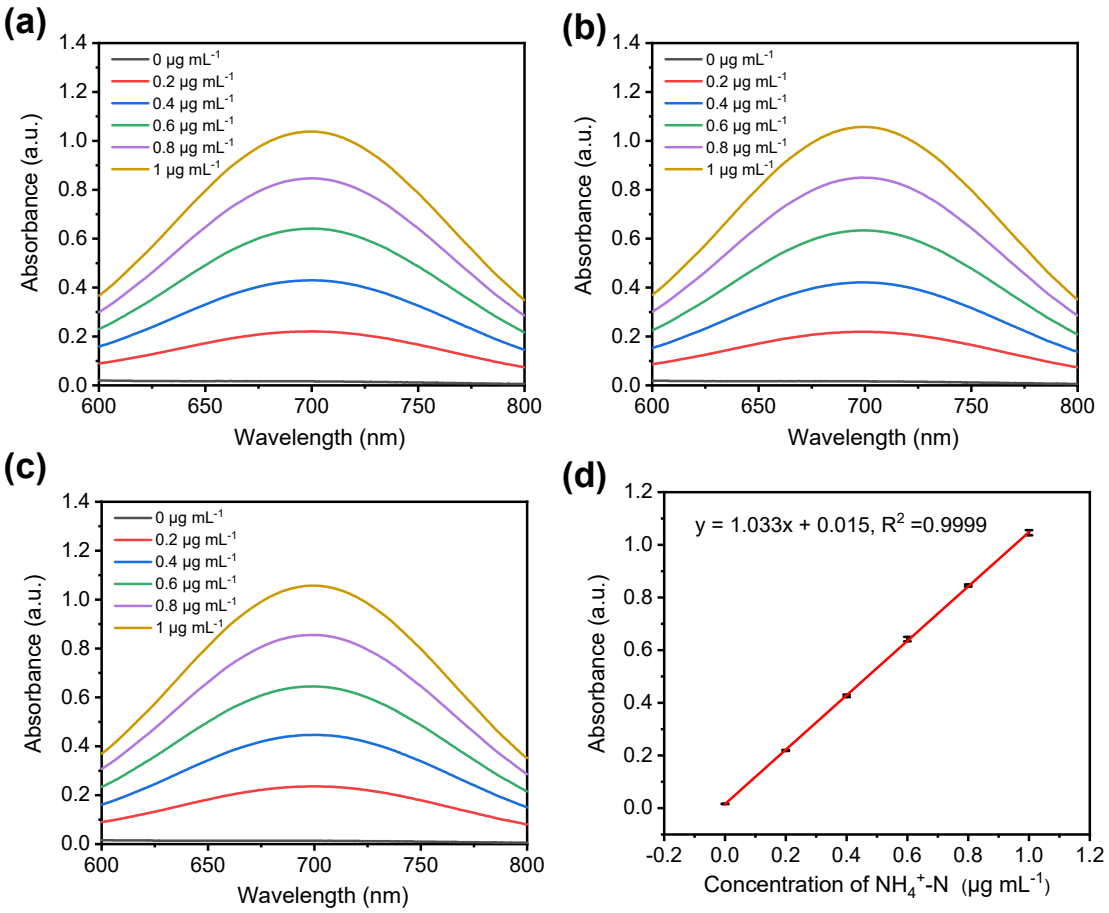

Fig. S12 (a-c) UV-Vis absorption spectra of various NH_4^+-N concentrations for three repeated experiments. (d) Calibration curve used for estimation of NH_4^+-N concentration.

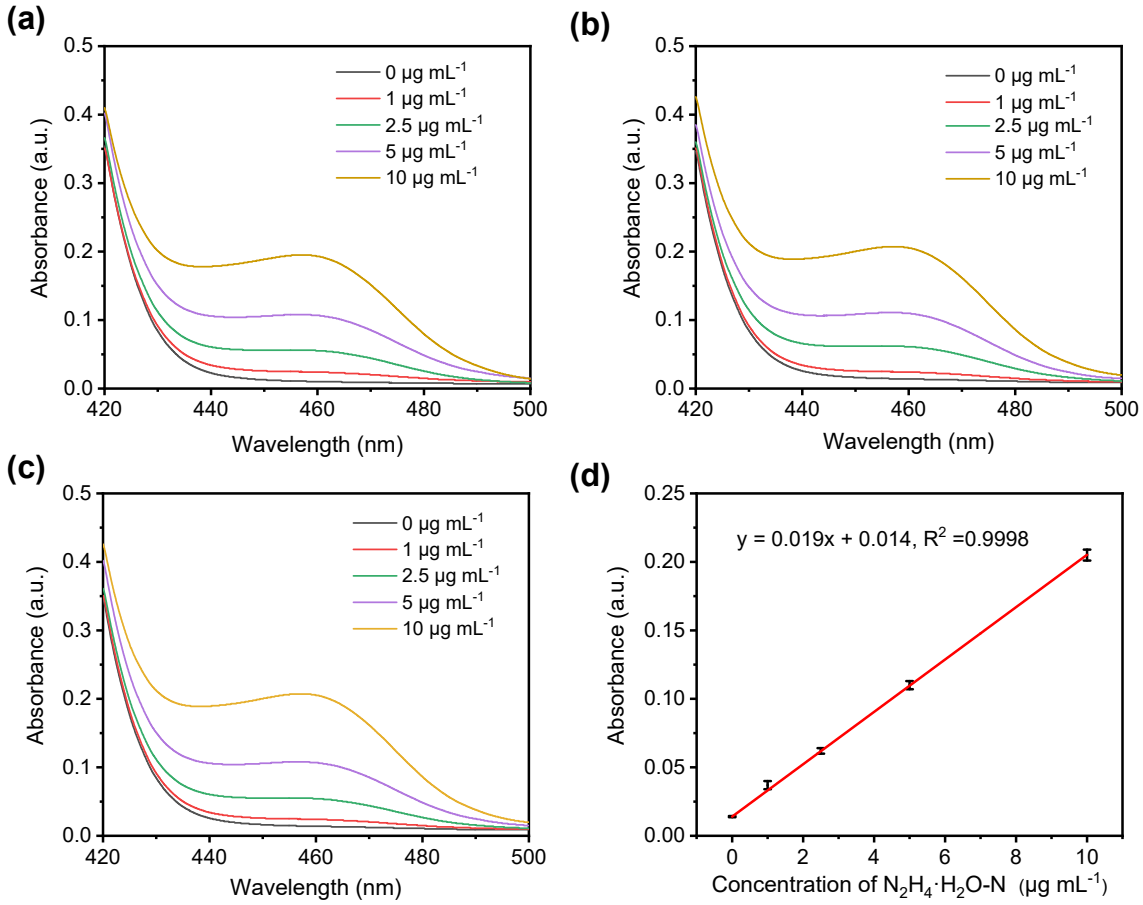

Fig. S13 (a-c) UV-Vis absorption spectra of the various concentrations of $N_2H_4 \cdot H_2O$ for three replicated tests. (d) The calibration curve used for calculation of $N_2H_4 \cdot H_2O$ concentration.

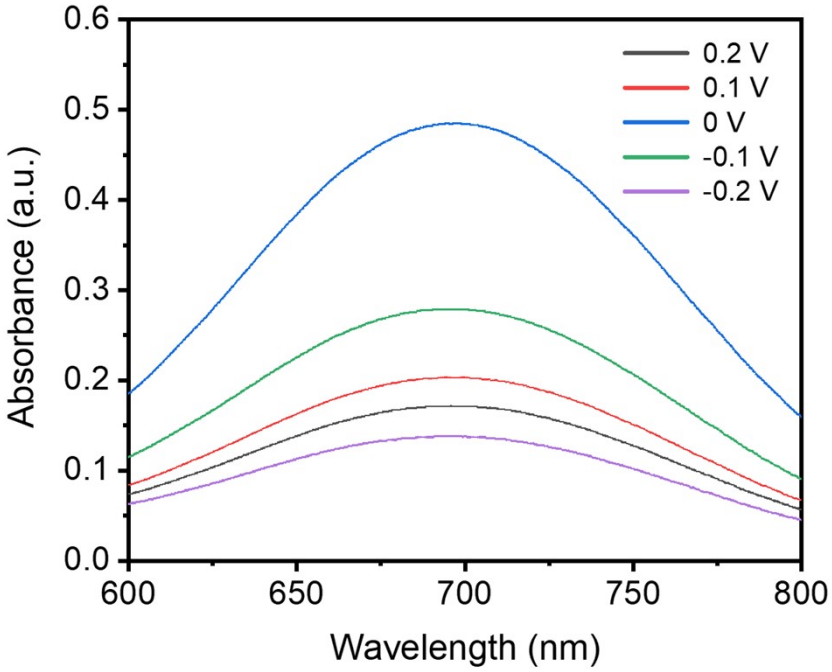

Fig. S14 UV-Vis absorption spectra of NH_4^+-N concentration at different applied potentials.

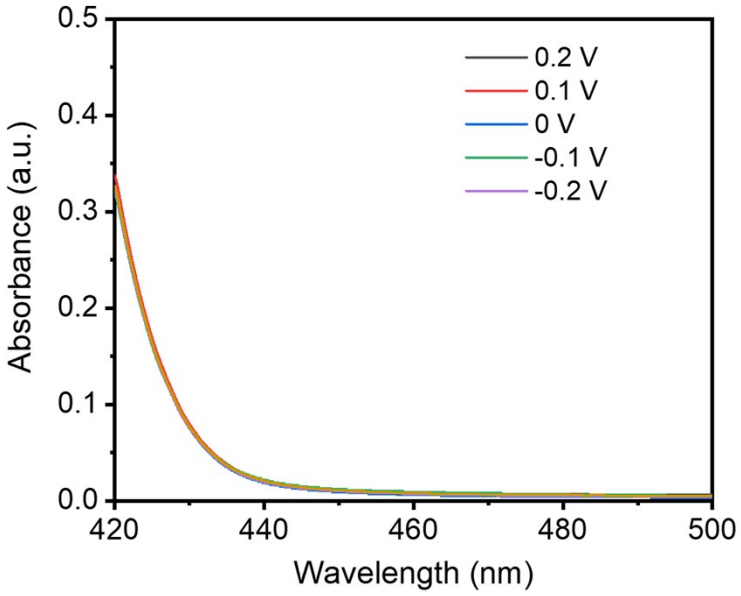

Fig. S15 UV-Vis absorption spectra of collected samples obtained at different applied potentials for $N_2H_4 \cdot H_2O$ detection.

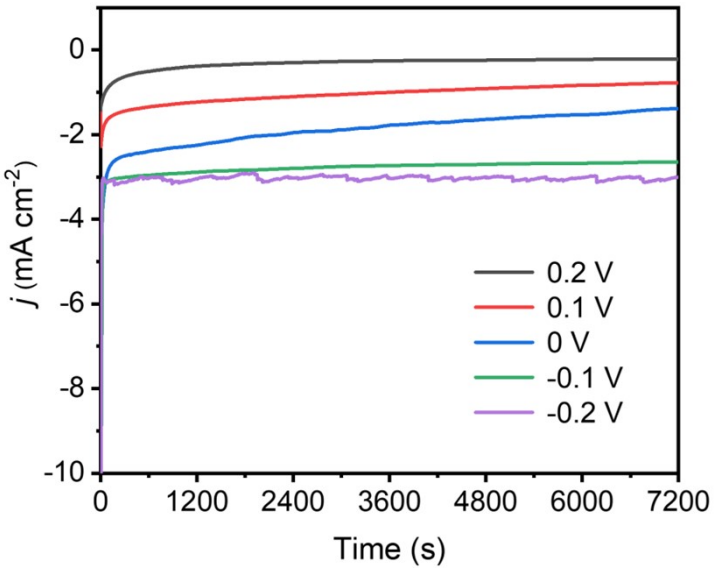

Fig. S16 Chronoamperometry curves in plasma treated 1.0 M KOH for 2 h of eNO_2^-RR at different applied potentials.

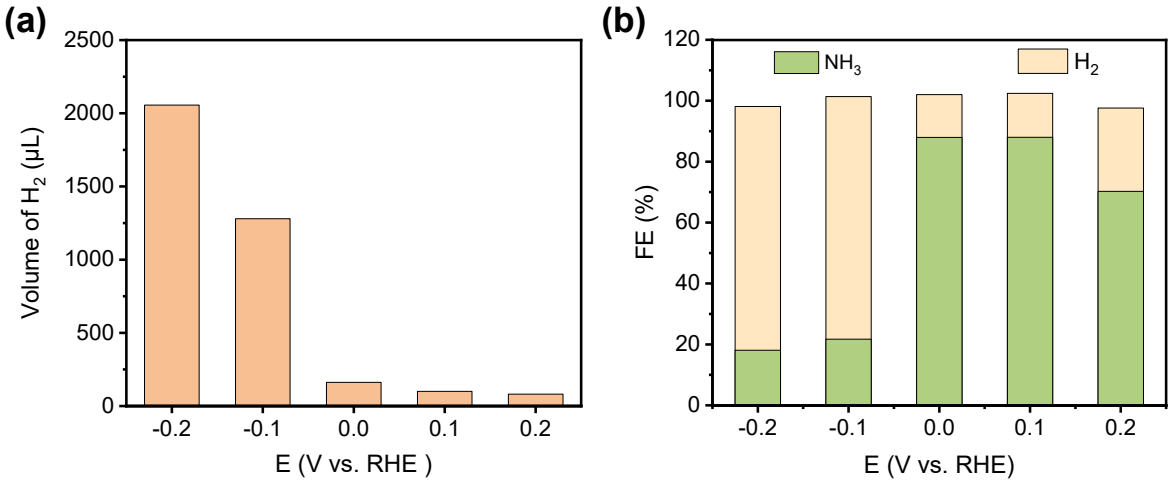

Fig. S17 (a) Volume of H_2 detected by gas chromatography method at different applied potentials. (b) FEs of different products at different applied potentials.

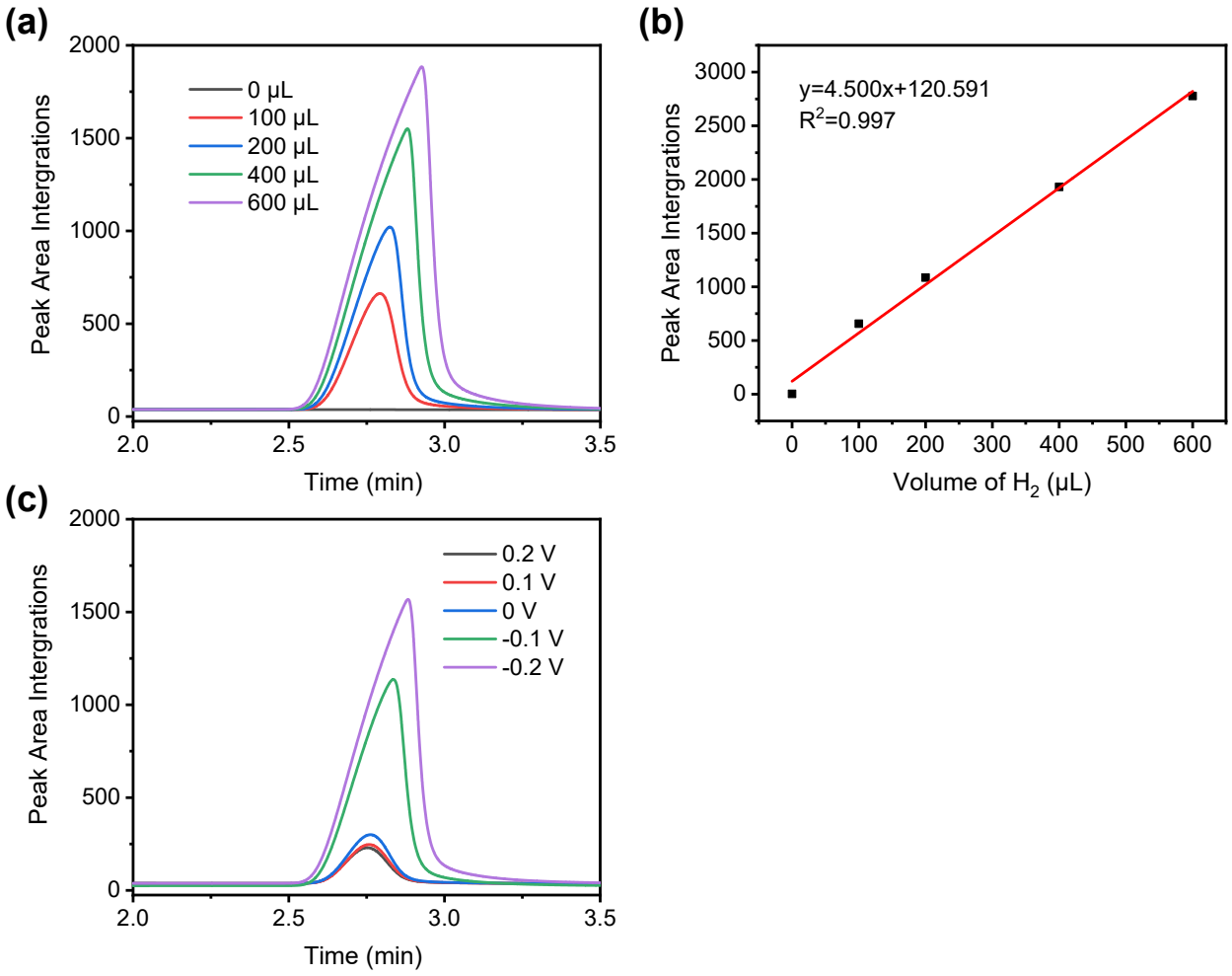

Fig. S18 (a) Gas chromatography spectra of the various volume of H_2. (b) The calibration curve used for calculation of H_2 volume. (c) Gas chromatography spectra of H_2 volume at different applied potentials.

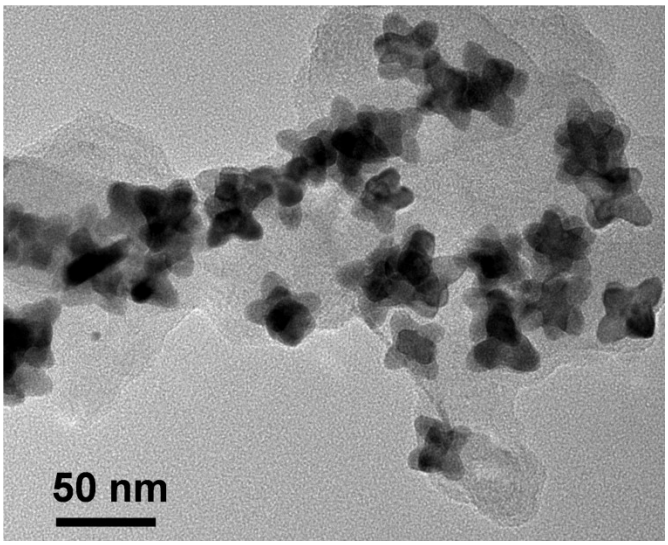

Fig. S19 TEM image of the PtCu HPs catalyst after long-time stability test.

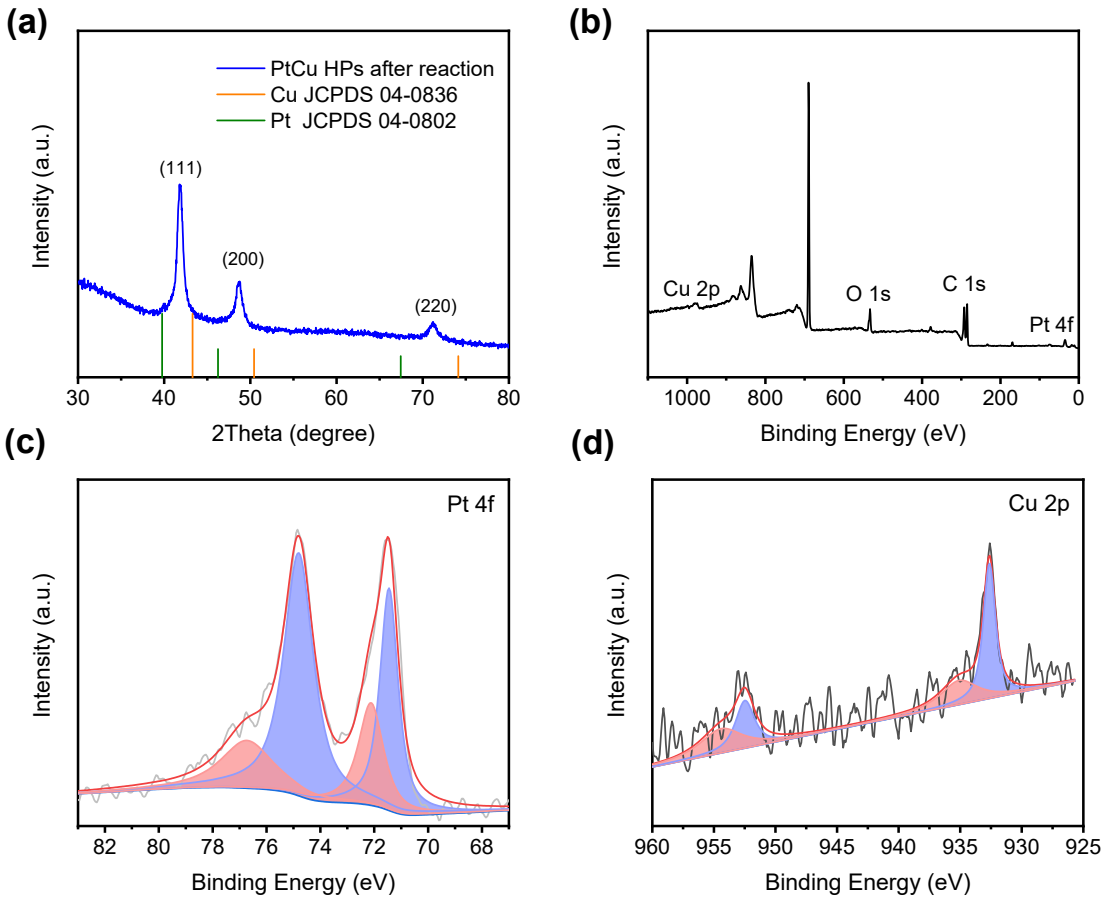

Fig. S20 (a) XRD pattern of PtCu HPs after long-time stability test. (b) Surface survey XPS spectrum of PtCu HPs. High-resolution (c) Pt 4f and (d) Cu 2p spectra of PtCu HPs after long-time stability test.

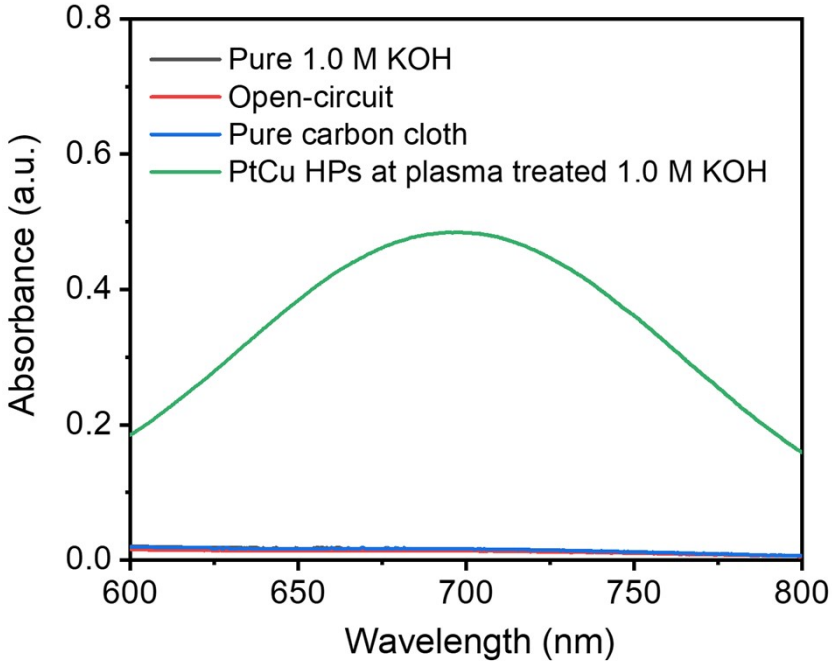

Fig. S21 UV-Vis absorption spectra of collected samples under different control conditions for NH_3 detection.

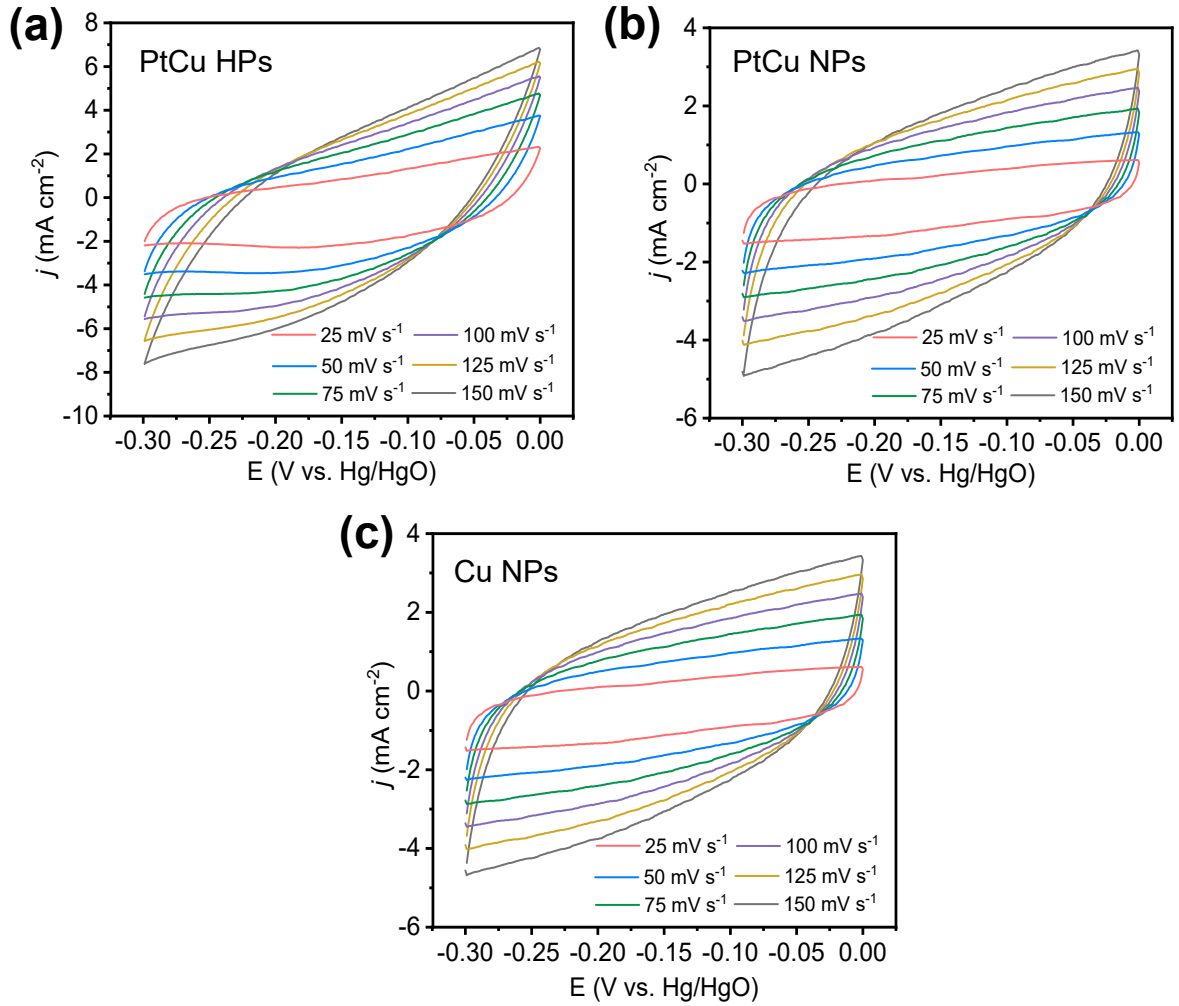

Fig. S22 Cyclic voltammetry curves of (a) PtCu HPs, (b) PtCu NPs and (c) Cu NPs with various scan rates (25, 50, 75, 100, 125, 150 mV s^{-1}) in the region of 0 V to -0.30 V (vs. Hg/HgO).

Tab. S1 Comparison results of our work with recently reported works for plasma generated NO_x^-.

Plasma	Feeding gas	Gas flowing rate	Absorption liquid	NO_x^- yield rate	Ref.
Gliding arc and microwave tandem plasma	Air	45 L min^{-1}	1.0 M KOH (200 mL)	98.16 mmol h^{-1}	This work
Nanosecond pulsed spark plasma	N_2+O_2	40 mL min^{-1}	0.1 M KOH (100 mL)	1.35 mmol h^{-1}	1
Pulsed high voltage discharge plasma	N_2+O_2	30 mL min^{-1}	0.1 M KOH (30 mL)	0.468mmol h^{-1}	2
Spark discharge plasma	Air	50 mL min^{-1}	0.1 M KOH (30 mL)	0.045 mmol h^{-1} (NO_2^-)	3
Double reactor glow and spark discharge plasma	Air	2 L min^{-1}	10 mM H_2SO_4 (100 mL)	2.97 mmol h^{-1}	4
Rotating gliding arc plasma jet	Air	7 L min^{-1}	0.1 M KOH (100 mL)	9.06 mmol h^{-1}	5
Jet-type plasma with Ti bubbler	Air	25 L min^{-1}	1.0 M NaOH (500 mL)	55.29 mmol h^{-1}	6
Gliding arc plasma	Air	9 L min^{-1}	0.1 M KOH (100 mL)	28 mmol h^{-1} (NO_2^-)	7

Tab. S2 The comparable results of our work and other recently reported eNO_3^-RR, eNO_2^-RR and eNRR electrocatalysts.

Catalysts	Conditions	NH_3 Yield Rate	FE (%)	Ref.
PtCu HPs	Plasma treated 1.0 M KOH	166.02 μg h^{-1} mg^{-1} (0 V vs. RHE)	84.37	This work
Ni_3B@$NiB_{2.74}$	0.10 M KOH + 100 mM NO_2^-	198.3 mmol h^{-1} cm^{-2} (-0.3V vs. RHE)	~100	1
Cu NWs	Plasma treated 10 mM H_2SO_4	45 nmol s^{-1} cm^{-2} (-0.5V vs. RHE)	~100	4
Co SAs/N-C	Plasma treated 0.1 M KOH	~3.0 mg h^{-1} cm^{-2} (-0.63V vs. RHE)	~62	5
Ru-Cu NW/CF	0.1 M PBS + 500 ppm NO_2^-	211.73 mg h^{-1} cm^{-2} (-0.6 V vs. RHE)	94.1	8
Pd/CuO NOs	0.1 M K_2SO_4 + 0.01 M KNO_2	906.4 μg h^{-1} mg^{-1} (-1.5 V vs. SCE)	91.8	9
MnO_2 NA/TM	0.1 M NaOH + 0.1 M $NaNO_2$	6300 μg h^{-1} mg^{-1} (-0.8 V vs. RHE)	65.4	10
Ni_2P nanosheet array	0.1 M PBS+200 ppm NO_2^-	2692.2 ± 92.1 μg h^{-1} cm^{-2} (-0.3 V vs. RHE)	90.2 ± 3.0	11
CoB@TiO_2/TP	0.1 M Na_2SO_4+200 ppm $NaNO_2$-N	233.1 μmol h^{-1} cm^{-2} (-0.7 V vs. RHE)	95.2	12
NiFe LDH/Vulcan	0.5 M Na_2SO_4+ 50 mM $NaNO_2$	351 μg h^{-1} mg^{-1} (-1.0 V vs. RHE)	85	13
PdCu/Cu_2O	0.5 M Na_2SO_4+100 ppm NO_3^--N	0.19 mmol h^{-1} cm^{-2} (-0.4 V vs. RHE)	94.32	14
Cu-N-C (SAC)	0.05 M K_2SO_4 +50 ppm NO_3^-	1.15 μg h^{-1} mg^{-1} (-0.95 V vs. RHE)	19.5	15
Fe-N-C (SAC)	0.1 M K_2SO_4 + 0.5 M NO_3^-	5245 μg h^{-1} mg^{-1} (-0.66 V vs. RHE)	75	16
PTCDA/O-Cu	0.1 M PBS +500 ppm NO_3^-	33.54 μg h^{-1} mg^{-1} (-0.40 V vs. RHE)	77	17
Cu (111) nanosheets	0.1 M KOH + 10 mM KNO_3	390.1 μg h^{-1} mg^{-1} (-0.15 V vs. RHE)	99.7	18
Strained Ru	1 M KOH + 1.0 M	5.56 mol g^{-1} h^{-1}	~100%	19

nanoclusters	KNO_3	(-0.2 V vs. RHE)		
Cu@C	1 M KOH + 1×10^{-3} M NO_3^-	469.5 μg h^{-1} cm^{-2} (-0.9 V vs. RHE)	72	20
RuNi-MOF	0.5 M Na_2SO_4+50 ppm NO_3^--N	274 mg h^{-1} mg^{-1} (-1.6 V vs. Ag/AgCl)	73	21
$NiCo_2O_4$/CC	0.1 M NaOH + 0.1 M $NaNO_3$	973.2 μmol h^{-1} cm^{-2} (-0.6 V vs. RHE)	99 (-0.3 V vs RHE)	22
$BiFeO_3$	0.1 M KOH + 0.1 M KNO_3	90.45 mg h^{-1} mg^{-1} (-0.6 V vs. RHE)	96.85	23
Cu/Cu_2O NWAs	0.5 M Na_2SO_4+200 ppm NO_3^--N	0.245 mmol h^{-1} cm^{-2} (-0.85 V vs. RHE)	95.8 (-0.2 V vs RHE)	24
Pd_3Cu_1	1.0 M KOH + N_2	39.9 μg h^{-1} mg^{-1} (-0.25 V vs. RHE)	1.56 (-0.05 V vs RHE)	25
BiNi Alloy	0.1 M Na_2SO_4 + N_2	17.5 μg h^{-1} mg^{-1} (-0.3 V vs. RHE)	13.8	26
Fe_{SA}-NO-C-900	0.1 M HCl + N_2	31.9 μg h^{-1} mg^{-1} (-0.4 V vs. RHE)	11.8	27
NiFe-MOF	0.1 M $NaHCO_3$ + N_2	9.3 μg h^{-1} mg^{-1} (-0.345 V vs. RHE)	11.5	28
Mo_2C/C	0.5 M Li_2SO_4 + N_2 (pH =2)	11.3 μg h^{-1} mg^{-1}_{Mo2C} (-0.3 V vs. RHE)	7.8	29
MoS_2 QDs	0.5 M $LiClO_4$ + N_2	39.6 μg h^{-1} mg^{-1} (-0.3 V vs. RHE)	12.9	30
CoS_2@NC	0.1 M HCl + N_2	17.45 μg h^{-1} mg^{-1} (-0.15 V vs. RHE)	4.6	31
PdRu	0.1 M HCl + N_2	34.2 μg h^{-1} mg^{-1} (-0.2 V vs. RHE)	2.4	32

Tab. S3 The comparable results of reported NH_3 production rate, energy requirements and CO_2 emissions for the proposed method with H-B technology and other competing emerging technologies.

Nitrogen fixation method	NH_3 production rate (mg/h)	Energy requirement (kWh/kg_{NH3})	CO_2 emissions (t_{CO2}/t_{NH3})	Ref.
plasma-electrocatalysis integrated strategy	0.166	551.76	~0	This work
Plasma electrolytic	0.05	560000	~0	33
Packed-bed DBD	0.0081	340	~0	34
DBD jet electrolytic	0.44	2270	~0	35
Li-intermediary NRR	0.013	1731	~0	36
Li-intermediary NRR	0.48	1380000	~0	37
eNRR	0.00135	37	~0	38
eNRR	0.0083	5.5	~0	39
eNRR	0.0063	32	~0	40
eNRR	0.00264	29.92	~0	41
Fe–cat. (KM1) [a] (Haber-Bosch process)	642.6	10~13	~1.5	42

a. Cat. = 0.2 g, H_2:N_2= 3:1, WHSV= 60 000 mL g^{-1} h^{-1}, T= 400 °C, P= 10 MPa.

References

1. L. Li, C. Tang, X. Cui, Y. Zheng, X. Wang, H. Xu, S. Zhang, T. Shao, K. Davey and S. Z. Qiao, Efficient nitrogen fixation to ammonia through integration of plasma oxidation with electrocatalytic reduction, *Angew. Chem. Int. Ed. Engl.*, 2021, **60**, 14131-14137.
2. Y. Ren, C. Yu, L. Wang, X. Tan, Z. Wang, Q. Wei, Y. Zhang and J. Qiu, Microscopic-level insights into the mechanism of enhanced NH_3 synthesis in plasma-enabled cascade N_2 oxidation–electroreduction system, *J. Am. Chem. Soc.*, 2022, **144**, 10193-10200.
3. S.-L. Meng, C. Zhang, C. Ye, J.-H. Li, S. Zhou, L. Zhu, X.-B. Li, C.-H. Tung and L.-Z. Wu, Cobaloximes: selective nitrite reduction catalysts for tandem ammonia synthesis, *Energy Environ. Sci.*, 2023, **16,** 1590-1596.
4. J. Sun, D. Alam, R. Daiyan, H. Masood, T. Zhang, R. Zhou, P. J. Cullen, E. C. Lovell, A. Jalili and R. Amal, A hybrid plasma electrocatalytic process for sustainable ammonia production, *Energy Environ. Sci.*, 2021, **14**, 865-872.
5. A. Wu, J. Yang, B. Xu, X.-Y. Wu, Y. Wang, X. Lv, Y. Ma, A. Xu, J. Zheng, Q. Tan, Y. Peng, Z. Qi, H. Qi, J. Li, Y. Wang, J. Harding, X. Tu, A. Wang, J. Yan and X. Li, Direct ammonia synthesis from the air via gliding arc plasma integrated with single atom electrocatalysis, *Appl. Catal., B*, 2021, **299**, 120667.
6. Z. Meng, J.-X. Yao, C.-N. Sun, X. Kang, R. Gao, H.-R. Li, B. Bi, Y.-F. Zhu, J.-M. Yan and Q. Jiang, Efficient ammonia production beginning from enhanced air activation, *Adv. Energy Mater.*, 2022, **12**, 2202105.
7. J. Zheng, H. Zhang, J. Lv, M. Zhang, J. Wan, N. Gerrits, A. Wu, B. Lan, W. Wang, S. Wang, X. Tu, A. Bogaerts and X. Li, Enhanced NH_3 synthesis from air in a plasma tandem-electrocatalysis system using plasma-engraved N-doped defective MoS_2, *JACS Au*, 2023, **3**, 1328-1336.
8. N. Q. Tran, L. T. Duy, D. C. Truong, B. T. Nguyen Le, B. T. Phan, Y. Cho, X. Liu and H. Lee, Efficient ammonia synthesis via electroreduction of nitrite using single-atom Ru-doped Cu nanowire arrays, *Chem. Commun.*, 2022, **58**, 5257-5260.
9. S. Liu, L. Cui, S. Yin, H. Ren, Z. Wang, Y. Xu, X. Li, L. Wang and H. Wang, Heterointerface-triggered electronic structure reformation: Pd/CuO nano-olives motivate nitrite electroreduction to ammonia, *Appl. Catal., B*, 2022, **319**, 121876.
10. X. He, X. Li, X. Fan, J. Li, D. Zhao, L. Zhang, S. Sun, Y. Luo, D. Zheng, L. Xie, A. M. Asiri, Q. Liu and X. Sun, Ambient electroreduction of nitrite to ammonia over Ni nanoparticle supported on molasses-derived carbon sheets, *ACS Appl. Nano Mater.*, 2022, **5**, 14246-14250.

11. G. Wen, J. Liang, L. Zhang, T. Li, Q. Liu, X. An, X. Shi, Y. Liu, S. Gao, A. M. Asiri, Y. Luo, Q. Kong and X. Sun, Ni_2P nanosheet array for high-efficiency electrohydrogenation of nitrite to ammonia at ambient conditions, *J. Colloid Interface Sci.*, 2022, **606**, 1055-1063.
12. J. Chen, X. He, J. Li, X. Li, Z. Cai, Y. Luo, D. Zheng, T. Li, Y. Wang, Q. Liu, S. Sun, A. Farouk, M. S. Hamdy, X. Sun and B. Ying, Three-dimensional porous Co foam with nanosheets subunits for high-performance electrocatalytic nitrate-to-ammonia conversion, *Inorg. Chem. Front.*, 2023, DOI: 10.1039/D3QI00718A.
13. W. Wang and E. C. M. Tse, Enhanced nitrite electrovalorization to ammonia by a NiFe layered double hydroxide, *Eur. J. Inorg. Chem.*, 2022, **2022**, e202200291.
14. H. Yin, Z. Chen, S. Xiong, J. Chen, C. Wang, R. Wang, Y. Kuwahara, J. Luo, H. Yamashita, Y. Peng and J. Li, Alloying effect-induced electron polarization drives nitrate electroreduction to ammonia, *Chem. Catal.*, 2021, **1**, 1088-1103.
15. T. Zhu, Q. Chen, P. Liao, W. Duan, S. Liang, Z. Yan and C. Feng, Single-atom Cu catalysts for enhanced electrocatalytic nitrate reduction with significant alleviation of nitrite production, *Small*, 2020, **16**, 2004526.
16. Z.-Y. Wu, M. Karamad, X. Yong, Q. Huang, D. A. Cullen, P. Zhu, C. Xia, Q. Xiao, M. Shakouri, F.-Y. Chen, J. Y. Kim, Y. Xia, K. Heck, Y. Hu, M. S. Wong, Q. Li, I. Gates, S. Siahrostami and H. Wang, Electrochemical ammonia synthesis via nitrate reduction on Fe single atom catalyst, *Nat. Commun.*, 2021, **12**, 2870.
17. G.-F. Chen, Y. Yuan, H. Jiang, S.-Y. Ren, L.-X. Ding, L. Ma, T. Wu, J. Lu and H. Wang, Electrochemical reduction of nitrate to ammonia via direct eight-electron transfer using a copper–molecular solid catalyst, *Nat. Energy*, 2020, **5**, 605-613.
18. X. Fu, X. Zhao, X. Hu, K. He, Y. Yu, T. Li, Q. Tu, X. Qian, Q. Yue, M. R. Wasielewski and Y. Kang, Alternative route for electrochemical ammonia synthesis by reduction of nitrate on copper nanosheets, *Appl. Mater. Today*, 2020, **19**, 100620.
19. J. Li, G. Zhan, J. Yang, F. Quan, C. Mao, Y. Liu, B. Wang, F. Lei, L. Li, A. W. M. Chan, L. Xu, Y. Shi, Y. Du, W. Hao, P. K. Wong, J. Wang, S.-X. Dou, L. Zhang and J. C. Yu, Efficient ammonia electrosynthesis from nitrate on strained ruthenium nanoclusters, *J. Am. Chem. Soc.*, 2020, **142**, 7036-7046.
20. Z. Song, Y. Liu, Y. Zhong, Q. Guo, J. Zeng and Z. Geng, Efficient electroreduction of nitrate into ammonia at ultralow concentrations via an enrichment effect, *Adv. Mater.*, 2022, **34**, 2204306.

21. J. Qin, K. Wu, L. Chen, X. Wang, Q. Zhao, B. Liu and Z. Ye, Achieving high selectivity for nitrate electrochemical reduction to ammonia over MOF-supported RuxOy clusters, *J. Mater. Chem. A*, 2022, **10**, 3963-3969.
22. Q. Liu, L. Xie, J. Liang, Y. Ren, Y. Wang, L. Zhang, L. Yue, T. Li, Y. Luo, N. Li, B. Tang, Y. Liu, S. Gao, A. A. Alshehri, I. Shakir, P. O. Agboola, Q. Kong, Q. Wang, D. Ma and X. Sun, Ambient ammonia synthesis via electrochemical reduction of nitrate enabled by $NiCo_2O_4$ nanowire array, *Small*, 2022, **18**, 2106961.
23. J. Wang, D. Wu, M. Li, X. Wei, X. Yang, M. Shao and M. Gu, Bismuth ferrite as an electrocatalyst for the electrochemical nitrate reduction, *Nano Lett.*, 2022, **22**, 5600-5606.
24. Y. Wang, W. Zhou, R. Jia, Y. Yu and B. Zhang, Unveiling the activity origin of a copper-based electrocatalyst for selective nitrate reduction to ammonia, *Angew. Chem. Int. Ed. Engl.*, 2020, **59**, 5350-5354.
25. F. Pang, Z. Wang, K. Zhang, J. He, W. Zhang, C. Guo and Y. Ding, Bimodal nanoporous Pd_3Cu_1 alloy with restrained hydrogen evolution for stable and high yield electrochemical nitrogen reduction, *Nano Energy*, 2019, **58**, 834-841.
26. Z. Fang, P. Wu, Y. Qian and G. Yu, Gel-derived amorphous bismuth–nickel alloy promotes electrocatalytic nitrogen fixation via optimizing nitrogen adsorption and activation, *Angew. Chem. Int. Ed. Engl.*, 2021, **60**, 4275-4281.
27. J. Yao, Y. Zhou, J.-M. Yan and Q. Jiang, Regulating $Fe_2(MoO_4)_3$ by Au nanoparticles for efficient N_2 Electroreduction under ambient conditions, *Adv. Energy Mater.*, 2021, **11**, 2003701.
28. J. Duan, Y. Sun, S. Chen, X. Chen and C. Zhao, A zero-dimensional nickel, iron–metal–organic framework (MOF) for synergistic N_2 electrofixation, *J. Mater. Chem. A*, 2020, **8**, 18810-18815.
29. H. Cheng, L.-X. Ding, G.-F. Chen, L. Zhang, J. Xue and H. Wang, Nitrogen reduction reaction: molybdenum carbide nanodots enable efficient electrocatalytic nitrogen fixation under ambient conditions, *Adv. Mater.*, 2018, **30**, 1870350.
30. W. Ye, M. Arif, X. Fang, M. A. Mushtaq, X. Chen and D. Yan, Efficient photoelectrochemical route for the ambient reduction of N_2 to NH_3 based on nanojunctions assembled from MoS_2 Nanosheets and TiO_2, *ACS Appl. Mater. Interfaces*, 2019, **11**, 28809-28817.
31. P. Wei, H. Xie, X. Zhu, R. Zhao, L. Ji, X. Tong, Y. Luo, G. Cui, Z. Wang and X. Sun, CoS_2 nanoparticles-embedded N-doped carbon nanobox derived from ZIF-67 for electrocatalytic N_2-to-NH_3 fixation under ambient conditions, *ACS Sustainable Chem. Eng.*, 2020, **8**, 29-33.

32. H. Wang, Y. Li, D. Yang, X. Qian, Z. Wang, Y. Xu, X. Li, H. Xue and L. Wang, Direct fabrication of bi-metallic PdRu nanorod assemblies for electrochemical ammonia synthesis, *Nanoscale*, 2019, **11**, 5499-5505.
33. S. Kumari, S. Pishgar, M. E. Schwarting, W. F. Paxton and J. M. Spurgeon, Synergistic plasma-assisted electrochemical reduction of nitrogen to ammonia. *Chem. Commun.*, 2018, **54**, 13347–13350.
34. Y. Wang, M. Craven, X. Yu, J. Ding, P. Bryant, J. Huang and X. Tu, Plasma-enhanced catalytic synthesis of ammonia over a Ni/Al_2O_3 catalyst at near-room temperature: Insights into the importance of the catalyst surface on the reaction mechanism. *ACS Catal.*, 2019, **9**, 10780–10793.
35. R. Hawtof, S. Ghosh, E. Guarr, C. Xu, R. Mohan Sankaran and J. N. Renner, Catalyst-free, highly selective synthesis of ammonia from nitrogen and water by a plasma electrolytic system. *Sci. Adv.*, 2019, **5**, eaat5778.
36. S. Z. Andersen, V. Čolić, S. Yang, J. A. Schwalbe, A. C. Nielander, J. M. McEnaney, K. Enemark-rasmussen, J. G. Baker, A. R. Singh and B. A. Rohr, A rigorous electrochemical ammonia synthesis protocol with quantitative isotope measurements. *Nature*, 2019, **570**, 504–508.
37. N. Lazouski, Z. J. Schiffer, K. Williams and K. Manthiram, Understanding continuous lithium-mediated electrochemical nitrogen reduction. *Joule*, 2019, **3**, 1127–1139.
38. J. Wang, L. Yu, L. Hu, G. Chen, H. Xin and X. Feng, Ambient ammonia synthesis via palladium-catalyzed electrohydrogenation of dinitrogen at low overpotential. *Nat. Commun.*, 2018, **9**, 1795.
39. S.-J. Li, D. Bao, M.-M. Shi, B.-R. Wulan, J.-M. Yan and Q. Jiang, Amorphizing of Au nanoparticles by CeO_x–RGO hybrid support towards highly efficient electrocatalyst for N_2 reduction under ambient conditions. *Adv. Mater.*, 2017, **29**, 1700001.
40. L. Zhang, L.-X. Ding, G.-F. Chen, X. Yang, and H. Wang, Ammonia synthesis under ambient conditions: selective electroreduction of dinitrogen to ammonia on black phosphorus nanosheets. *Angew. Chem. Int. Ed. Engl.*, 2019, **58**, 2612–2616.
41. B. H. R. Suryanto, D. Wang, L. M. Azofra, M. Harb, L. Cavallo, R. Jalili, D. R. G. Mitchell, M. Chatti and D. R. MacFarlane, MoS_2 polymorphic engineering enhances selectivity in the electrochemical reduction of nitrogen to ammonia. *ACS Energy Lett.*, 2019, **4**, 430–435.
42. S. Hagen, R. Barfod, R. Fehrmann, C. J. H. Jacobsen, H. T. Teunissen, and I. Chorkendorff, Ammonia synthesis with barium-promoted iron−cobalt alloys supported on carbon. *J. Catal.*, 2003, **214**, 327−335.